

# Dissecting X-Ray-Emitting Gas Around the Center of Our Galaxy

Q. D. Wang,<sup>1,2\*</sup> M. A. Nowak<sup>3</sup>, S. B. Markoff<sup>4</sup>, F. K. Baganoff<sup>3</sup>,  
 S. Nayakshin<sup>5</sup>, F. Yuan<sup>6</sup>, J. Cuadra<sup>7</sup>, J. Davis<sup>3</sup>, J. Dexter<sup>8</sup>,  
 A. C. Fabian<sup>1</sup>, N. Grosso<sup>9</sup>, D. Haggard<sup>10</sup>, J. Houck<sup>3</sup>, L. Ji<sup>11</sup>, Z. Li<sup>12</sup>,  
 J. Neilsen<sup>13,3</sup>, D. Porquet<sup>9</sup>, F. Ripple<sup>2</sup>, R. V. Shcherbakov<sup>14</sup>

<sup>1</sup>Institute of Astronomy, University of Cambridge, Madingley Road, Cambridge CB3 0HA, UK.

<sup>2</sup>Department of Astronomy, University of Massachusetts, Amherst, MA 01003, USA.

<sup>3</sup>Kavli Institute for Astrophysics and Space Research,  
 Massachusetts Institute of Technology, Cambridge MA 02139, USA.

<sup>4</sup>Astronomical Institute, “Anton Pannekoek”, University of Amsterdam,  
 Postbus 94249, 1090 GE, Amsterdam, The Netherlands.

<sup>5</sup>Department of Physics and Astronomy, University of Leicester, Leicester LE1 7RH, UK.

<sup>6</sup>Shanghai Astronomical Observatory, CAS, 80 Nandan Road, Shanghai 200030, China

<sup>7</sup> Instituto de Astrofísica, Pontificia Universidad Católica de Chile, Chile.

<sup>8</sup>Theoretical Astrophysics Center and Department of Astronomy,  
 University of California, Berkeley, CA 94720-3411, USA

<sup>9</sup>Observatoire Astronomique de Strasbourg, Université de Strasbourg,  
 CNRS, UMR 7550, Strasbourg, France

<sup>10</sup>CIERA Fellow, Center for Interdisciplinary Exploration and Research in Astrophysics,  
 Department of Physics and Astronomy, Northwestern University, Evanston, IL 60208, USA

<sup>11</sup>Purple Mountain Observatory, CAS, Nanjing, 210008, P.R. China.

<sup>12</sup>School of Astronomy and Space Science, Nanjing University, Nanjing, 210093, China.

<sup>13</sup>Einstein Fellow, Boston University, Boston, MA 02215, USA.

<sup>14</sup>Hubble Fellow; Department of Astronomy, University of Maryland, College Park, MD 20742-2421, USA.

\*To whom correspondence should be addressed; E-mail: wqd@astro.umass.edu.

**Most supermassive black holes (SMBHs) are accreting at very low levels and are difficult to distinguish from the galaxy centers where they reside. Our own Galaxy’s SMBH provides a uniquely instructive exception, and we present a close-up view of its quiescent X-ray emission based on 3 mega-second of *Chandra* observations. Although the X-ray emission is elongated and aligns well with a surrounding disk of massive stars, we can rule out a concentration of low-mass coronally active stars as the origin of the**

**emission based on the lack of predicted Fe K $\alpha$  emission. The extremely weak H-like Fe K $\alpha$  line further suggests the presence of an outflow from the accretion flow onto the SMBH. These results provide important constraints for models of the prevalent radiatively inefficient accretion state.**

The nucleus of our Galaxy offers a multitude of unique opportunities for observing the interplay between a SMBH and its immediate surroundings. The SMBH, named Sgr A\*, has a mass of  $4.1 \times 10^6 M_\odot$  (1,2), and at its distance of 8 kpc (1), an arcsecond (1'') subtends  $1.2 \times 10^{17}$  cm, or  $1.0 \times 10^5 r_s$ , where  $r_s = 1.2 \times 10^{12}$  cm is the Schwarzschild radius. The X-ray emission of Sgr A\* typically has an unabsorbed 2-10 keV luminosity ( $L_x$ ) of a few times  $10^{33}$  erg s $^{-1}$  (3), or a factor of  $\sim 10^{11}$  lower than the canonical maximum allowed (Eddington) luminosity of the SMBH, representing a common ‘‘inactive’’ state of galactic nuclei in the Local Universe. Because of its proximity, Sgr A\* allows us to study this extremely low- $L_X$  state in unparalleled detail [e.g., (4,5)].

It is believed that Sgr A\* feeds off the winds from surrounding massive stars (6–8). At the so-called Bondi capture radius  $r_B \sim 4''(T_a/10^7 \text{ K})^{-1}$  (9), the gravitational pull of the SMBH wins over the expanding motion of the medium with effective temperature  $T_a$ . The corresponding Bondi capture rate is estimated to be  $\dot{M}_B \sim 1 \times 10^{-5} M_\odot \text{ yr}^{-1}$  [e.g., (3)]. If Sgr A\* indeed accretes at this rate and if the 10% X-ray emission efficiency of a ‘‘normal’’ active galactic nucleus applies, one would predict a luminosity of  $L_x \sim 10^{41}$  erg s $^{-1}$ . That the observed  $L_x$  is nearly a factor of  $\sim 10^8$  smaller has led to a renaissance of radiatively inefficient accretion flow (RIAF) models (10,11), including self-similar solutions (12–17) and numerous hydrodynamic or magneto-hydrodynamic simulations of various complexities and dynamic ranges [e.g., (18–23)]. Many of the recent model development were stimulated by sub-mm polarization/Faraday rotation measurements, providing stringent constraints on the accretion rate in the innermost region ( $r \lesssim 10^2 r_s$ ) of Sgr A\* [e.g., (24)]. But controversies remain as to which model (if any) may apply [e.g., (19,21)].

High-angular resolution observations of Sgr A\* – such as those provided by the *Chandra* X-ray Observatory — can in principle probe the accretion phenomenon not only in its innermost regions, but also the outer boundary conditions at flow onset. However, there are substantial uncertainties regarding the interpretation of the quiescent emission of Sgr A\* which previous *Chandra* observations showed to be extended with an intrinsic size of about 1.4'' (3). How that emission is distributed within this region, and how much is due to a bound accretion flow versus other components, remain unclear. Furthermore, it has been proposed (3,25) that a substantial or even dominant fraction of the emission could arise from a centrally-peaked population of coronally active, low-mass main-sequence stars around Sgr A\*, which is allowed by current near-infrared observations. This scenario predicts a 6.4 keV emission line with the equivalent width (EW) in the range of 50 – 100 eV, due to fluorescence of photospheric weakly ionized irons, irradiated by coronal flare X-rays. It is thus essential to test this hypothesis before we can assign the X-ray emission to the accretion flow onto the SMBH.

We use data taken during the Sgr A\* X-ray Visionary Program [XVP; (26)]. The ACIS-S (Advanced

CCD Imaging Spectrometer-Spectroscopy), combined with the HETG (High-energy Transmission Grating), was placed at the aim point of the telescope. The on-axis spatial resolution of *Chandra* is  $\sim 0.4''$  (FWHM), whereas the spectral resolution of the 0th-order ACIS-S/HETG data is about a factor of  $\sim 2$  better than that of the previous ACIS-I observations and thus enables critical spectroscopic diagnostics of the X-ray emission.

These observations reveal X-ray emission from Sgr A\* that appears substantially more extended than a point-like source [Fig. 1a; (26)]. After subtracting a point-like contribution, which accounts for 20% of the total quiescent emission (26), an east-west-elongated X-ray enhancement emerges around Sgr A\* on  $\sim 1''$ - $1.5''$  scales (Fig. 1b). This relatively symmetric enhancement morphologically resembles the so-called clockwise stellar disk, which is the most notable kinematically organized structure known for the massive stars around Sgr A\* (27,28). Irregular low-surface-brightness features (e.g., spurs toward the north-east and south-east; Fig. 1b) appear on scales greater than the enhancement, but still roughly within the Bondi radius. These features are softer (more prominent in the 1-4 keV band than in the 4-9 keV band) than the smoothly-distributed background.

The quiescent X-ray emission is also spectrally distinct from the point-like flare emission (26), which is considerably harder. The accumulated flare spectrum can be well characterized by a power law with photon index 2.6(2.2, 3.0), and a foreground absorption with an equivalent hydrogen column density of  $N_H = 16.6(14.1, 19.4) \times 10^{22} \text{ cm}^{-2}$  [see (29) for the definition of the uncertainties], consistent with the previous analysis of individual bright flares (30,31). Because of the simplicity of the flare spectrum, this  $N_H$  measurement can be considered a reliable estimate of the foreground X-ray-absorbing column density along the sightline toward Sgr A\*, and hence a useful constraint in modeling the more complex spectrum of the quiescent X-ray emission.

By contrast, the quiescent spectrum shows prominent emission lines (Fig. 2). In addition to the previously known Fe  $K\alpha$  emission at  $\sim 6.7$  keV,  $K\alpha$  lines of several other species (He- and H-like Ar, He-like S and Ca), as well as He-like Fe  $K\beta$  are also apparent. We find that a single-temperature (1-T) plasma with metal abundance set equal to zero describes the overall (continuum) shape of the observed spectrum well, while individual Gaussians can be used to characterize the centroid, flux, and EW of six most significant emission lines [Fig. 2a; (26)]. There is little sign of the diagnostic  $K\alpha$  emission lines from neutral/weakly ionized Fe at  $\sim 6.4$  keV or H-like Fe at 6.97 keV.

We can reject the stellar coronal hypothesis, based on our temporal, spatial, and spectral results. First, our spectrum does not confirm the presence of the 6.4-keV line, previously suggested by (25). Measuring the 6.4-keV line, which is adjacent to the strong highly ionized Fe  $K\alpha$  line, is difficult when the spectral resolution is poor, as was the case for the previous ACIS-I spectrum, because the measurement then depends sensitively on the assumed thermal plasma model. Our measured upper limit to the EW of the 6.4-keV line emission, 22 eV (26), is more than a factor of 2 below the range predicted before (25). Second, the quiescent emission shows no significant variation on time scales of hours or days, as expected from the sporadic giant coronal flares of individual stars. Third, if the bulk of the quiescent emission is

due to stellar coronal activity, then it should also account for some of the detected X-ray flares, especially the relatively long and weak ones (25). However, no sign of any line emission, even the strong Fe  $K\alpha$  line, is found in any flare spectra [individual or accumulated; (26,32)]. Fourth, the spatial distribution of the weak flares is as point-like as the strong ones, in contrast to the extended quiescent emission (26). Therefore, we conclude that neither flare nor quiescent emission originates from stellar coronal activity, although the latter could still give a small ( $\lesssim 25\%$ ) contribution to the quiescent emission.

As described above, the diffuse X-ray emission on the scale of  $\lesssim 1.5''$  (or  $1.5 \times 10^5 r_s$ ) morphologically resembles a gaseous disk with inclination angle and line-of-nodes similar to those of the stellar disk around Sgr A\*. This scale, a factor of  $\gtrsim 2$  smaller than  $r_B$ , corresponds to the sound-crossing distance over  $\sim 10^2 (T_a/10^7 \text{ K})^{-1/2}$  years (where  $T_a$  is the ambient gas temperature), which is about the time since the last major burst of Sgr A\*, as inferred from X-ray light echoes [e.g., (33,34)]. The burst, making Sgr A\* a factor of  $\sim 10^6$  brighter than its present state over a period of several  $10^2$  years, could have substantially altered the surroundings, as well as the accretion flow itself. A stable accretion flow would then need to be re-established gradually, roughly at the sound-crossing speed. This flow would be expected to carry the net angular momentum of the captured wind material with an orientation similar to that of the stars, which could explain the morphological similarities. However, the recent hydrodynamic simulations of the stellar wind accretion (8) suggest that a Keplerian motion-dominated flow should occur on much smaller scales ( $r \lesssim 0.1''$ ). If true, then the plasma on larger scales must be supported mainly by large gradients of thermal, magnetic, cosmic-ray, and/or turbulence pressures, and/or the motion must be strongly affected by the outward transport of angular momentum from the accretion flow, as indicated in various simulations [e.g., (19)].

One can further use the relative strengths of individual lines as powerful diagnostics of the accretion flow (35,36). X-ray emission lines trace the emission measure distribution as a function of plasma temperature. The ionic fraction of He-like S (S XV), for example, peaks at  $kT \sim 1.4 \text{ keV}$ , while the He-like Fe dominates in the temperature range of  $\sim 1.5 - 7 \text{ keV}$  and the H-like Fe peaks sharply at  $\sim 9 \text{ keV}$ . At temperatures  $\gtrsim 12 \text{ keV}$ , Fe becomes nearly fully ionized. Thus if the radial dependence of the temperature can be modeled, the density or mass distribution as a function of radius can be inferred.

The extremely weak H-like Fe  $K\alpha$  line in the Sgr A\* spectrum immediately suggests a RIAF with a very low mass fraction of the plasma at  $kT \gtrsim 9 \text{ keV}$ , or a strong outflow at radii  $r \gtrsim 10^4 r_s$  (26). Radially resolved analysis further shows that the X-ray spectrum becomes increasingly hard with decreasing radius and that the line centroid and EW of the Fe  $K\alpha$  line also changes with the radius. These characteristics can naturally be explained by the presence of plasma at a relatively low temperature in the region, consistent with the onset of the RIAF from captured stellar wind material at  $r \sim 10^5 r_s$ .

As detailed in (26), we can quantitatively check the consistency of the X-ray spectrum of the quiescent Sgr A\* with various RIAF solutions. In particular, we can reject (with a null hypothesis probability of  $10^{-6}$ ) a no-outflow solution (i.e., a constant mass accretion rate along the accretion flow leading to a radial plasma density profile  $n \propto r^{-3/2+s}$ , in which  $s = 0$ ). This solution substantially over-predicts

the H-like Fe  $K\alpha$  line, while other lines are not fully accounted for. The predicted shape of the model spectrum is also far too flat, resulting in a substantially reduced  $N_H [= 8.0(7.6, 8.3) \times 10^{22} \text{ cm}^{-2}]$ , inconsistent with other estimates. Therefore, the no-outflow solution can be firmly rejected, both statistically and physically.

We find that a *RIAF* model with a flat radial density profile (i.e.,  $s \sim 1$ ) provides an excellent fit to both the continuum and lines data (Fig. 2b), and gives estimates of both the plasma metal abundance and the foreground absorption column consistent with other independent measurements (26). With this fit, we can infer the radial emission structure of the accretion flow. Although the line emission is dominated by the outer, cooler region of the *RIAF* ( $r \gtrsim 10^4 r_s$ ), the innermost hot component contributes primarily to the continuum emission, mostly via bremsstrahlung processes. We find that this latter contribution accounts for only  $\lesssim 20\%$  of the observed quiescent X-ray luminosity (consistent with the spatially decomposed fraction), in stark contrast to the  $s = 0$  solution, whose X-ray emission is completely dominated by the innermost regions ( $r \lesssim 10^2 r_s$ ).

Further insight into the physical processes involved in the *RIAF* can be obtained from comparing our X-ray measurements, most sensitive to the outer radial density profile, with existing constraints on the accretion properties in the innermost region. For example, submillimeter Faraday rotation measurements (24) set a lower limit to the accretion rate of  $2 \times 10^{-9} M_\odot \text{ yr}^{-1}$  into the innermost region. Assuming that a large fraction of the Bondi accretion rate,  $\dot{M}_B \sim 1 \times 10^{-5} M_\odot \text{ yr}^{-1}$ , initially ends up in the *RIAF* at a radius  $\sim 10^5 r_s$ , then an  $s \sim 1$  density profile can exist down to radius  $r_i \sim 10^2 r_s$ . This  $s \sim 1$  density profile over a broad radial range is consistent with various *RIAF* solutions [e.g., (14,17)] and numerical simulations [e.g., (18)]. The Faraday rotation measurements also yield an upper limit to the accretion rate of  $2 \times 10^{-7} M_\odot \text{ yr}^{-1}$ , assuming that the magnetic field is near equipartition, ordered, and largely radial in the *RIAF* (24). With this upper limit, assuming that  $r_i \sim 10^2 r_s$  we can infer  $s > 0.6$  and hence  $\theta \gtrsim 0.6$  for the radial temperature profile  $T \propto r^{-\theta}$  of the *RIAF*. This constraint on  $\theta$  places a fundamental limit on thermal conduction-induced heat outflow (37).

The flat density profile of the flow (i.e.,  $s \sim 1$ ) suggests the presence of an outflow that nearly balances the inflow (26). As a result,  $\lesssim 1\%$  of the matter initially captured by the SMBH reaches the innermost region around Sgr A\*, limiting the accretion power to  $\lesssim 10^{39} \text{ erg s}^{-1}$ . Much of this power is probably used to drive the outflow, which could affect the environment of the nuclear region and even beyond [e.g., (38)]. This combination of the low energy generation and high consumption rates of Sgr A\* naturally explains its low bolometric luminosity (a few times  $10^{36} \text{ erg s}^{-1}$ ) and its lack of powerful jets. Observations of nearby elliptical galaxies with jet-inflated cavities in diffuse X-ray-emitting gas reveal a relation between the jet and Bondi accretion powers (in units of  $10^{43} \text{ erg s}^{-1}$ ),  $P_{jet} \approx 0.007 P_{Bondi}^{1.3}$ , where  $P_{Bondi}$  is assumed to have a 10% efficiency of the Bondi mass accretion rate (39). We speculate that the nonlinearity of this relation is due to increasing outflow rates with decreasing Bondi power, leading to a reduced energy generation rate in the innermost region around a SMBH, where jets are launched. Extrapolating the relation down to the case for Sgr A\*, we may expect a jet to Bondi power

ratio of only  $\sim 0.2\%$ , consistent with the above inferred fractional mass loss due to the outflow.

The progress in understanding the accretion flow characteristics and orientation for our closest SMBH will lead to key constraints for the modeling of such phenomena in general. For Sgr A\* specifically these results will impact models of the “shadow” of the SMBH [e.g., (40,41)], which can be measured by very long baseline interferometry at (sub)millimeter wavelengths (42), and the radiation from hydrodynamic interactions of orbiting stars [e.g., S2; (43)] and the G2 object with ambient media at distances down to  $\sim 10^3 r_s$  from the SMBH [e.g., (44)].

## References and Notes

1. A. M. Ghez, *et al.*, *ApJ* **689**, 1044 (2008).
2. S. Gillessen, *et al.*, *ApJ* **692**, 1075 (2009).
3. F. K. Baganoff, *et al.*, *ApJ* **591**, 891 (2003).
4. R. Genzel, F. Eisenhauer, S. Gillessen, *Reviews of Modern Physics* **82**, 3121 (2010).
5. S. Markoff, *Proceedings of the National Academy of Science* **107**, 7196 (2010).
6. R. F. Coker, F. Melia, *ApJ* **488**, L149 (1997).
7. E. Quataert, R. Narayan, M. J. Reid, *ApJ* **517**, L101 (1999).
8. J. Cuadra, S. Nayakshin, F. Martins, *MNRAS* **383**, 458 (2008).
9. H. Bondi, *MNRAS* **112**, 195 (1952).
10. S. L. Shapiro, A. P. Lightman, D. M. Eardley, *ApJ* **204**, 187 (1976).
11. M. J. Rees, M. C. Begelman, R. D. Blandford, E. S. Phinney, *Nature* **295**, 17 (1982).
12. R. Narayan, I. Yi, *ApJ* **428**, L13 (1994).
13. R. Narayan, I. Yi, R. Mahadevan, *Nature* **374**, 623 (1995).
14. E. Quataert, A. Gruzinov, *ApJ* **539**, 809 (2000).
15. R. D. Blandford, M. C. Begelman, *MNRAS* **303**, L1 (1999).
16. R. D. Blandford, M. C. Begelman, *MNRAS* **349**, 68 (2004).
17. M. C. Begelman, *MNRAS* **420**, 2912 (2012).
18. F. Yuan, M. Wu, D. Bu, *ApJ* **761**, 129 (2012).

19. F. Yuan, D. Bu, M. Wu, *ApJ* **761**, 130 (2012).
20. J. Li, J. Ostriker, R. Sunyaev, *ApJ* **767**, 105 (2013).
21. R. Narayan, A. SAdowski, R. F. Penna, A. K. Kulkarni, *MNRAS* **426**, 3241 (2012).
22. S. Dibi, S. Drappeau, P. C. Fragile, S. Markoff, J. Dexter, *MNRAS* **426**, 1928 (2012).
23. S. Drappeau, S. Dibi, J. Dexter, S. Markoff, P. C. Fragile, *MNRAS* **431**, 2872 (2013).
24. D. P. Marrone, J. M. Moran, J.-H. Zhao, R. Rao, *ApJ* **654**, L57 (2007).
25. S. Sazonov, R. Sunyaev, M. Revnivtsev, *MNRAS* **420**, 388 (2012).
26. Supplementary materials of the paper .
27. T. Paumard, *et al.*, *ApJ* **643**, 1011 (2006).
28. J. R. Lu, *et al.*, *ApJ* **690**, 1463 (2009).
29. Parameter uncertainties in the brackets represent the 90% statistical confidence intervals or one-sided 95% limits .
30. D. Porquet, *et al.*, *A&A* **488**, 549 (2008).
31. M. A. Nowak, *et al.*, *ApJ* **759**, 95 (2012).
32. J. Nielsen et al., *ApJ in press* (2013).
33. R. Terrier, *et al.*, *ApJ* **719**, 143 (2010).
34. M. Nobukawa, S. G. Ryu, T. G. Tsuru, K. Koyama, *ApJ* **739**, L52 (2011).
35. R. Narayan, J. Raymond, *ApJ* **515**, L69 (1999).
36. R. Perna, J. Raymond, R. Narayan, *ApJ* **541**, 898 (2000).
37. R. V. Shcherbakov, F. K. Baganoff, *ApJ* **716**, 504 (2010).
38. R. M. Crocker, *MNRAS* **423**, 3512 (2012).
39. S. W. Allen, R. J. H. Dunn, A. C. Fabian, G. B. Taylor, C. S. Reynolds, *MNRAS* **372**, 21 (2006).
40. H. Falcke, F. Melia, E. Agol, *ApJ* **528**, L13 (2000).
41. M. Mościbrodzka, C. F. Gammie, J. C. Dolence, H. Shiokawa, P. K. Leung, *ApJ* **706**, 497 (2009).
42. S. S. Doeleman, *et al.*, *Nature* **455**, 78 (2008).

43. S. Nayakshin, *A&A* **429**, L33 (2005).
44. S. Gillessen, *et al.*, *ApJ* **763**, 78 (2013).
45. J. E. Davis, *ApJ* **562**, 575 (2001).
46. F. K. Baganoff, *et al.*, *Nature* **413**, 45 (2001).
47. Y.-D. Xu, R. Narayan, E. Quataert, F. Yuan, F. K. Baganoff, *ApJ* **640**, 319 (2006).
48. Q. D. Wang, F. J. Lu, E. V. Gotthelf, *MNRAS* **367**, 937 (2006).
49. K. A. Arnaud, *ADASS V*, G. H. Jacoby, J. Barnes, eds. (1996), vol. 101 of *ASP Conference Series*, p. 17.
50. A. R. Foster, L. Ji, R. K. Smith, N. S. Brickhouse, *ApJ* **756**, 128 (2012).
51. J. Wilms, A. Allen, R. McCray, *ApJ* **542**, 914 (2000).
52. D. A. Verner, G. J. Ferland, K. T. Korista, D. G. Yakovlev, *ApJ* **465**, 487 (1996).
53. R. Narayan, I. V. Igumenshchev, M. A. Abramowicz, *ApJ* **539**, 798 (2000).
54. F. Yuan, E. Quataert, R. Narayan, *ApJ* **598**, 301 (2003).
55. R. Narayan, A. C. Fabian, *MNRAS* **415**, 3721 (2011).
56. R. V. Shcherbakov, R. F. Penna, J. C. McKinney, *ApJ* **755**, 133 (2012).

**Acknowledgments:** We thank the Sgr A\* *Chandra* XVP Collaboration ([www.sgra-star.com/collaboration-members](http://www.sgra-star.com/collaboration-members)), which is supported by SAO grant GO2-13110A, and are grateful to *Chandra* Mission Planning for their support during our 2012 campaign. QDW thanks the hospitality of the Institute of Astronomy and the award of a Raymond and Beverley Sackler Distinguished Visitor fellowship. We acknowledge the role of the Lorentz Center, Leiden: the Netherlands Organization for Scientific Research Vidi Fellowship (639.042.711; SM). Further support from NASA was from Hubble Fellowship grant HST-HF-51298.01 (RVS); from Einstein Postdoctoral Fellowship grant PF2-130097 (JN); and from SAO contract SV3-73016 to MIT for support of the *Chandra* X-ray Center, which is operated by SAO for and on behalf of NASA under contract NAS8-03060; from CONICYT-Chile through FONDECYT (11100240), Basal (PFB0609) and Anillo (ACT1101) grants (JC); and from NSFC and the 973 Project (2009CB82400) of China (FY). The X-ray data used here are available from the *Chandra* archive at [asc.harvard.edu](http://asc.harvard.edu).



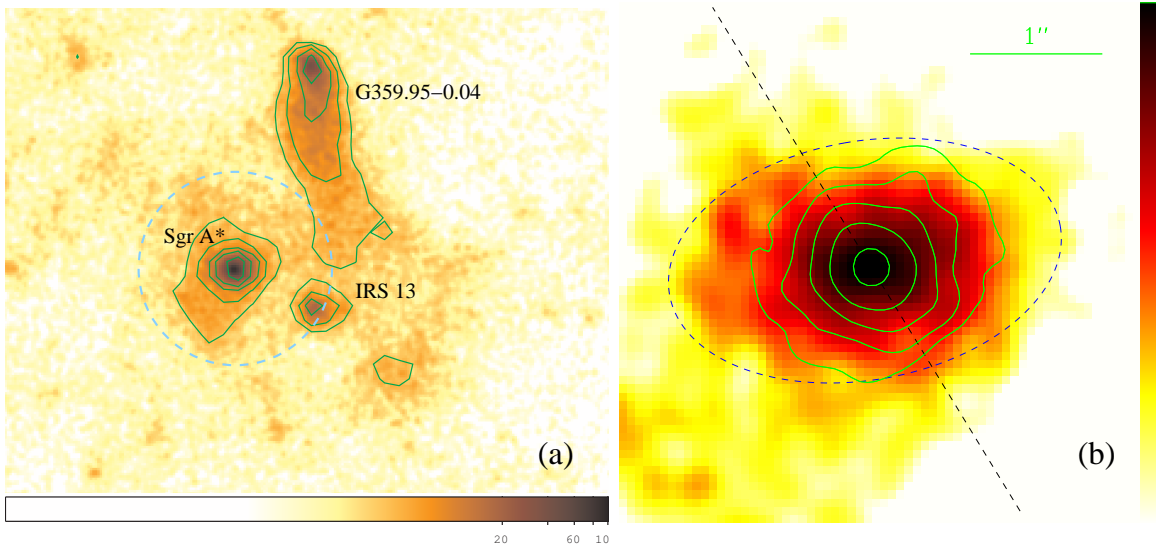


Figure 1: X-ray images of Sgr A\* in quiescence. (a) An image constructed with the XVP 0th-order ACIS-S/HETG data in the 1-9 keV band. The contours are at  $1.3, 2.2, 3.7, 6.3,$  and  $11 \times 10^{-4} \text{ cts s}^{-1} \text{ arcsec}^{-2}$ . North is up and East is to the left. The dashed circle around Sgr A\* marks its Bondi capture radius (assumed to be  $4''$ ). (b) A close-up of Sgr A\*. The emission is decomposed into extended (color image) and point-like (contour) components. The latter component is modeled with the net flare emission (26) and is illustrated as the intensity contours at 0.3, 0.6, 1.2, 2.4, and 5 counts per pixel. The straight dashed line marks the orientation of the Galactic plane, whereas the dashed ellipse of a  $1.5''$  semi-major axis illustrates the elongation of the primary massive stellar disk, which has an inclination of  $i \sim 127^\circ$ , a line-of-nodes position angle of  $100^\circ$  (East from North), and a radial density distribution  $\propto r^{-2}$  with a sharp inner cut off at  $r \approx 1''$  (27).

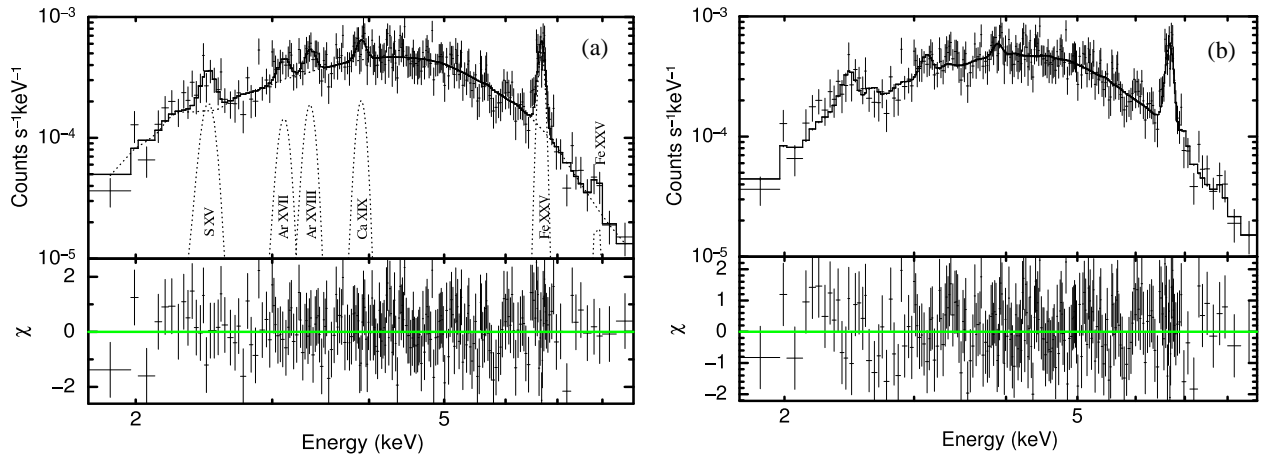


Figure 2: The X-ray spectrum of Sgr A\* in quiescence [extracted from the inner circle of  $1.5''$  radius and local-background-subtracted; (26)] and model fits: (a) zero-metallicity 1-T thermal bremsstrahlung continuum plus various Gaussian lines (Table S.1); (b) *RIAF* model with the best-fit  $\gamma = 2s/\theta = 1.9$ , where  $s$  and  $\theta$  are the indices parametrizing the density and temperature profiles, respectively (26).

## Supplementary Materials for Dissecting X-ray-emitting Gas around the Center of our Galaxy

Q. D. Wang, M. A. Nowak, S. B. Markoff, F. K. Baganoff, S. Nayakshin, F. Yuan, J. Cuadra, J. Davis, J. Dexter,  
A. C. Fabian, N. Grosso, D. Haggard, J. Houck, L. Ji, Z. Li, J. Neilsen, D. Porquet, F. Ripple, R. V. Shcherbakov  
correspondence to: wqd@astro.umass.edu

### **This PDF file includes:**

Materials and Methods

Figs. S1 to S3

Table S1

References (45-56)

### **Materials and Methods**

The *Chandra* X-ray Visionary Project (XVP) to observe the Milky Way's SMBH, Sgr A\*, and the surrounding inner few arcminutes, culminated in 38 observations for a total 3 mega-second exposure, taken during February 6 to October 29, 2012. This *Chandra* Cycle 13 program utilized the High Energy Transmission Gratings (HETG) in combination with the Advanced CCD Imaging Spectrometer-Spectroscopy (ACIS-S) to accomplish high spatial, spectral, and temporal resolutions. Only the 0th-order ACIS-S/HETG data from the observations are used in the present work. The spectral resolution of the data is about a factor of  $\sim 2$  better than that of the previous Advanced CCD Imaging Spectrometer-imaging (ACIS-I) observations (which suffered from a severe charge transfer inefficiency).

### Data Reduction

The data are reduced via standard CIAO processing routines (version 4.5; Calibration Database version 4.5.6). In particular, source detection is carried out for individual observations and later for the merged data set. Sources detected within  $3'$  of Sgr A\* and with position errors less than  $0.2''$  are used by the routine *reproject\_aspect* to match each observation to the longest one (ObsID 13842), which is aligned first to the radio position of Sgr A\* [J2000:  $RA = 17^h 45^m 40.041^s$ ,  $Dec = -29^\circ 00' 28.12''$ ]. The merged data can be treated approximately like a single observation, because the differences among the pointing directions of individual observations are all within a  $14''$  radius. Consistency checks for both spectral and spatial results have also been carried out with existing ACIS-I observations. We find no apparent calibration issues with the XVP ACIS-S/HETG data.

### Decomposition of the Sgr A\* data in the time domain

The data on Sgr A\* are divided into two parts: one in various flare periods and the other in “flare-free” or quiescent periods. A census of flares detected in the data can be found in (32). Different detection algorithms give slightly different properties (e.g., peak fluxes), as well as different numbers of flares, mostly at the low flux end. In this work, we have adopted the flare catalog from the detection with the “Bayesian Blocks” routine [see Appendix of (32)]. The catalog contains 45 flares, a few more than the number obtained with a Gaussian kernel detection scheme. Therefore, our adopted flare catalog leads to a relatively conservative definition of the quiescent X-ray emission. Various tests, such as auto-

correlation, suggest that the quiescent emission is nearly a pure Poisson process of a constant photon flux; the upper limit to the flare contribution to the emission within  $\lesssim 1.5''$  is 10%, consistent with the very flat fluence function of the detected flares (32). The total exposure is 0.18 mega-seconds for the flares and 2.78 mega-seconds for the quiescent emission. The data accumulated from the quiescent periods (after exposure correction) can be subtracted from those of the flare periods to obtain a net accumulated flare spectrum or image.

#### Flare image and spatial decomposition of the Sgr A\* quiescent X-ray emission

We construct an image of flares by stacking them and subtracting the exposure-corrected quiescent contribution. The three brightest ones are excluded from this stacking to minimize potential pile-up effects [two or more photons in a single “readout frame” being registered as a single event, or rejected as a non X-ray event; (45)] The resultant net flare image (represented by the contours in Fig. 1b) is consistent with the expected on-axis point-spread function of the instrument and shows a round morphology (with statistical noise). The radial intensity profile of the Sgr A\* flare emission is slightly narrower than that of J174538.05-290022.3 (Fig. S.2). The profile of this latter source is included here as a reference of a point-like distribution. The source shows high variability of X-ray intensity with time and is thus point-like. With a spectrum indicative of strong absorption and projected only  $27''$  west of Sgr A\* (Fig. S.1), the source is most likely located at the Galactic center or beyond. Therefore, the intensity profile of the source can reasonably be used as an empirical reference of the combined angular dispersion of X-ray radiation due to both the instrument point-spread function and the scattering by dust along the line of sight.

To better assess the extended morphology of the quiescent emission, we subtract from it the flare image scaled to minimize the roundness of the resultant image, but not to produce centrally depressed or peanut-shaped morphology. The adopted scaling corresponds to a subtracted point-like component accounting for 20% of the total quiescent emission — a fraction that is also consistent with the spectral decomposition of the emission to be described later.

#### Spectral analysis

We adopt the same  $1.5''$  radius region as used previously (25,46,47) to extract X-ray spectra of Sgr A\* in its flare and quiescent states. We also extract a “Sgr A\*-halo” spectrum from a concentric annulus of the inner and outer radii of  $2''$  and  $5''$ ; this outer bound is comparable to the Bondi radius within its uncertainty. The Sgr A\*-halo spectrum is not only used as the local background of the on-Sgr A\* spectrum, but analyzed to assess the ambient X-ray properties. To do so, we further obtain an “off-halo” spectral background from a concentric  $6''$ - $18''$  annulus (Fig. S.1). The comet-shaped pulsar wind nebula G359.95-0.04 (48), as well as the detected sources, are excluded from these annuli. Each on-source spectrum is grouped to achieve a respective background-subtracted signal-to-noise ratio of  $\gtrsim 3$ . The accurate background subtraction is only moderately important for the quiescent Sgr A\* spectrum. It has a 1-9 keV count rate of  $2.36 \times 10^{-3}$  counts  $s^{-1}$ ,  $\sim 25\%$  of which can attributed to the local background, as estimated in the Sgr A\*-halo region. This fraction would be reduced by a factor of  $\sim 2$ , if instead

the background estimated in the 6''-18'' annulus is used. Such a difference in the background subtraction would lead to some quantitative changes, but hardly affect the qualitative results presented in the present paper.

All our spectral fits are conducted with the XSPEC package [(49); version 12.8.0]; model names of the package are used unless otherwise noted. In particular, the spectrum of the optically-thin thermal plasma at a certain temperature is modeled with *APEC*, which uses the ATOMDB code (v2.0.1), assuming collisional ionization equilibrium (50). The metal abundances of the plasma, as well as the foreground X-ray-absorbing gas, are relative to the interstellar medium (ISM) values given in (51). The photoelectric absorption uses the Tuebingen-Boulder model [*TBABS*; (51)] with the cross-sections from (52). An alternative version of the plasma model (*VAPEC*) is sometimes used to allow for abundance variations of individual elements. Both the interstellar dust scattering (*DUSTSC*) and the CCD pile-up (*PILEUP*) effects (31) are also accounted for.

We use a simple 1-T optically-thin thermal plasma to characterize the X-ray spectrum of Sgr A\* in quiescence. To properly account for distinct emission line features in the spectrum, we allow the abundances of the relevant elements (S, Ar, Ca, and Fe, while all others are tied to C) to vary independently in the fit. This *VAPEC* model with  $kT = 3.5(3.0, 4.0)$  keV gives an acceptable fit to the spectrum ( $\chi^2/n.d.f. = 201/216$ ). But, the fitted  $N_H = 10.1(9.4, 11.1) \times 10^{22} \text{ cm}^{-2}$  is far too low to be consistent with that inferred from the flare spectral analysis. Therefore, the model is unlikely to be physical. Nevertheless, we find that the 1-T plasma with metal abundance set equal to zero gives a good (simple or “model-independent”) characterization of the spectral continuum. We can then use individual *Gaussians* to measure the emission lines (Fig. 2a). Table S.1 lists the fitted centroid, flux, EW, and identification for each of the six most significant lines. The table also includes upper limits to the fluxes and EWs of the diagnostic  $K\alpha$  emission lines from neutral/weakly ionized Fe and H-like Fe. Similar spectral analysis is also conducted for the Sgr A\*-halo region. The results are compared with those obtained for Sgr A\* in Fig. S.3) and in the main text.

#### Implement of the spectral model *RIAF*

While the quiescent X-ray spectrum obtained from the present work gives an unprecedented diagnostic capability to probe the accretion process of Sgr A\*, it is still not possible to discriminate among many possible spectral models or their combinations. Therefore, we primarily consider simple physical models, which capture key characteristics of the process. In particular, we test the *RIAF* solutions [e.g., (12,14,15,17,53,54)], by implementing a general spectral model for them. In such a solution, the inward radial motion as a function of the radius  $r$  is  $v_r = v_o(r_o/r)^{1/2}$ , or a fixed fraction of the Keplerian orbital velocity (the subscript  $_o$  is used to denote quantities at the outer radius  $r_o$ ); the accretion rate of the *RIAF* is  $\dot{M} = \dot{M}_o(r/r_o)^s$ , where a positive  $s$  would indicate a net mass loss or outflow from the flow. The mass conservation implies that the density profile is characterized by  $n = n_o(r_o/r)^{3/2-s}$ . The temperature is  $T = T_o(r_o/r)^\theta$ , increasing with decreasing radius due to the conversion of the gravitational potential energy into heat (i.e.,  $0 < \theta \leq 1$ ). These scaling relations have been largely confirmed

by various hydrodynamic and magneto-hydrodynamic simulations [e.g., (18,20)] as good approximations over broad radial ranges, although deviations may be expected at the accretion flow onset region near the Bondi radius [e.g., (47,55); considerably larger than our chosen  $r_o$ ] and in the innermost region ( $r_i \lesssim 10^2 r_s$ ), where the electron temperature becomes decoupled from the ion temperature [e.g., (18,56)]. We calculate the X-ray spectrum of this outer *RIAF* model by integrating the corresponding differential emission measure,  $dEM/d\log(T) \propto (T_o/T)^\gamma$  (where  $\gamma = 2s/\theta$ ), together with the emissivity function of the *APEC* plasma over the temperature range from  $T_o$  to  $T_i$ . The radiation from radii smaller than  $r_i$  is simply modeled with an independent bremsstrahlung component (*BREMSS*) at  $T_i$ .

#### RIAF model fit to the quiescent X-ray spectrum

The *RIAF* model constructed above gives an excellent fit to the spectrum, both globally ( $\chi^2/n.d.f. = 187/218$ ) and in terms of matching individual lines (Fig. 2b). The best-fit model gives  $\gamma = 1.9(1.4, 2.4)$ . If  $\theta \sim 1$  as typically assumed [e.g., (14,17)], this suggests a very flat density profile of the flow (i.e.,  $s \sim 1$ ), indicating an outflow mass-loss rate that nearly balances the inflow. The fitted metal abundance, 1.5(1.1, 2.1), and absorption column,  $13.8(12.2, 15.0) \times 10^{22} \text{ cm}^{-2}$ , are also consistent with their expected values. The shape of the bremsstrahlung spectrum (hence the fit) in the *Chandra* band is insensitive to the exact value of  $T_i$ . Its 95% lower limit is  $\sim 10^8 \text{ K}$ ; but the best fit value appears to go beyond the upper limit ( $\sim 10^9 \text{ K}$ ) of *APEC*. Thus, we fix  $T_i$  to this upper limit. The best-fit value and the one-sided 95% upper limit of  $T_o$  are  $0.96 \times 10^7 \text{ K}$  and  $1.5 \times 10^7 \text{ K}$ . No lower limit is given; the spectral contribution diminishes rapidly with decreasing temperature, because of the strong soft X-ray absorption along the sight line. We use the *CFLUX* convolution model to first estimate the unabsorbed luminosity of Sgr A\* in the 2-10 keV band as  $3.4(2.9, 4.3) \times 10^{33} \text{ erg s}^{-1}$ . We then estimate the luminosity of the *BREMSS* component to be 16(5, 23)% of the total flux of Sgr A\*. This fraction is consistent with the point source contribution obtained from the above spatial decomposition. The component should have approximately included the relatively small nonthermal contributions from undetected weak flares and photons inverse-Compton-scattered into the X-ray band in the very inner region of the accretion flow [e.g., (54)]. Therefore, we conclude that the fraction of the quiescent X-ray emission arises from the innermost region is about  $\sim 20\%$ .

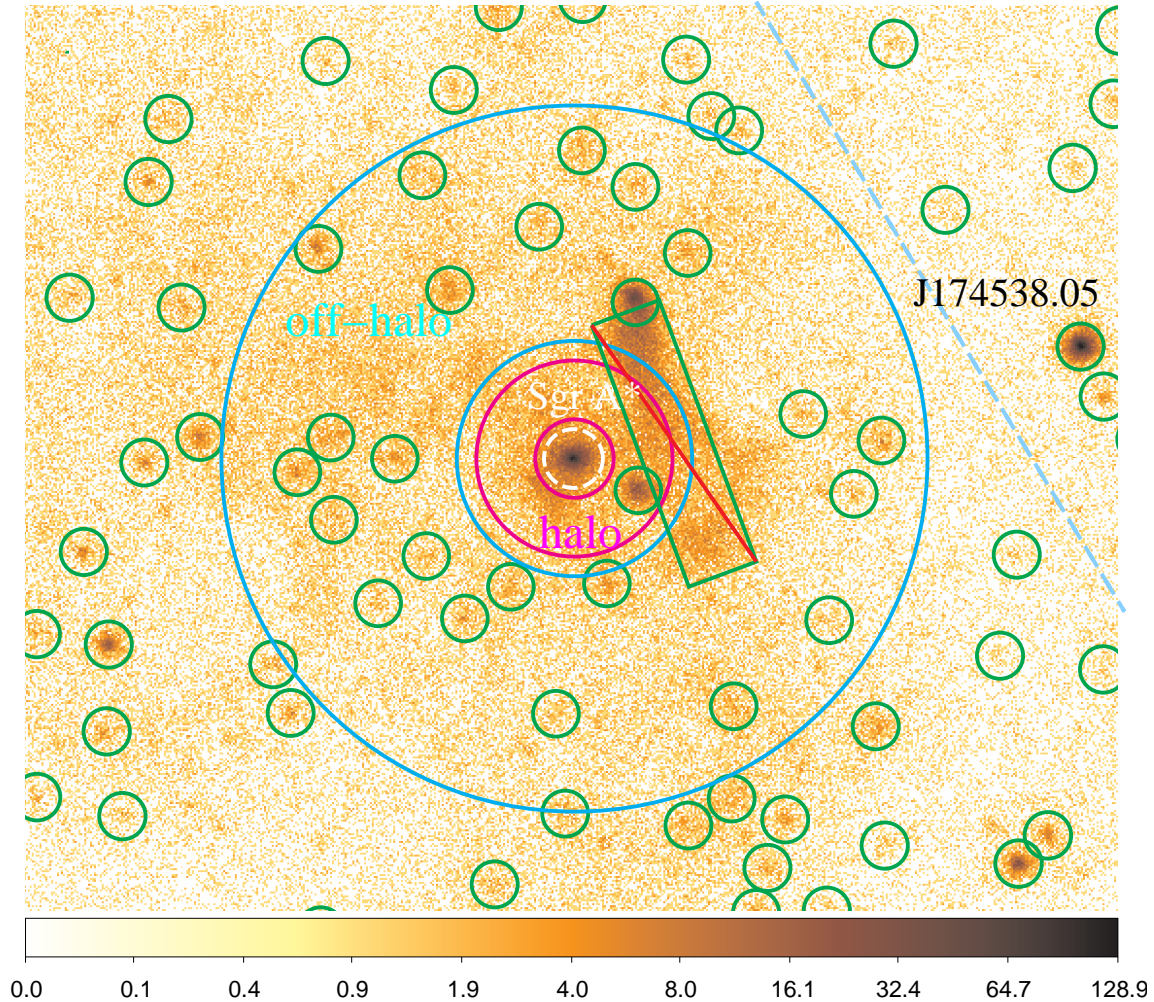


Figure S.1: X-ray Overview of the field ( $56'' \times 46''$ ) around Sgr A\*. The ACIS-S/HETG image is constructed in the same way as Fig. 1a. The small central (dashed white) circle marks the on-Sgr A\* spectral extraction region, while the two large concentric (solid magenta and cyan) annuli outline the Sgr A\*-halo and off-halo background subtraction regions. The green box and small circles mark areas that are significantly contaminated by an extended PWN and detected sources (1.5 times 70% energy-encircled radii) and are thus excluded from the spectral extractions.

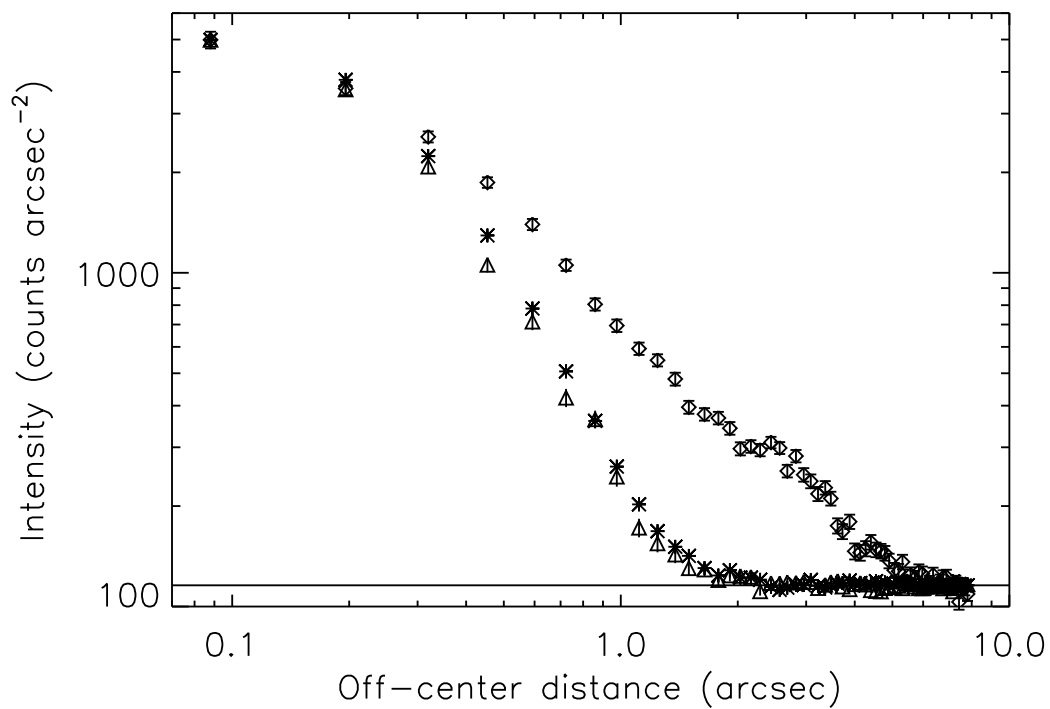


Figure S.2: Comparison of the radial 1-9 keV intensity profiles of Sgr A\* in quiescence (*diamonds*) and



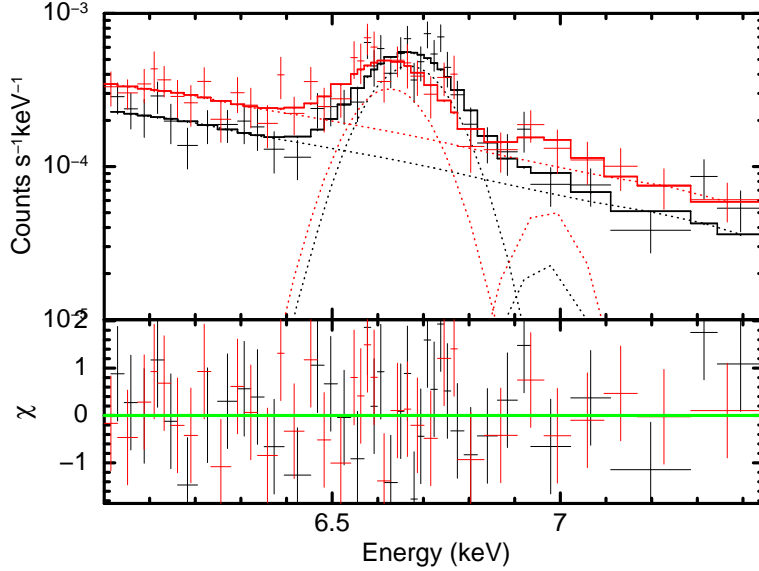


Figure S.3: Comparison between the quiescent X-ray spectrum of Sgr A\* (black; Fig. 2) and the Sgr A\*-halo spectrum (red; extracted from the 2''-5'' annulus; Fig. S.1) in the Fe K $\alpha$  complex region. Two Gaussian lines are added into the fit to characterize the 6.4 keV and 6.973 keV lines, although the best-fit model fluxes of the former line are zero for both spectra. the line centroid and EW of the Fe K $\alpha$  line in the spectrum of the Sgr A\*-halo region, 6.63(6.60 - 6.65) keV and 0.29(0.22 - 0.37) keV, are substantially different from those in the spectrum of Sgr A\*(Table S.1).

Table S.1: Measurements of individual emission lines

Line energy (keV)	flux ( $10^{-6}$ ph s $^{-1}$ cm $^{-2}$ )	EW (eV)	ID, expected energy (keV)
2.48 (2.44, 2.52)	2.5 (1.5, 3.8)	161 (101, 232)	S XV, 2.461
3.10 (3.03, 3.16)	0.6 (0.3, 1.0)	64 (27, 104)	Ar XVII, 3.140
3.35 (3.32, 3.39)	0.6 (0.3, 0.9)	72 (37, 109)	Ar XVIII, 3.32
3.91 (3.86, 3.94)	0.4 (0.2, 0.6)	63 (31, 96)	Ca XIX, 3.861
6.676 (6.660, 6.691)	1.2 (1.0, 1.4)	691 (584, 846)	Fe XXV, 6.675
7.874 (7.737, 8.012)	0.2 (0.03, 0.4)	181 (91, 417)	Fe XXV, 7.881
6.4 (fixed)	0 (0, 0.06)	0 (0, 22)	Fe I-XVII, 6.4
6.973 (fixed)	0.07 (0, 0.11)	0 (0, 42)	Fe XXVI, 6.973

Note: The dispersions of all the Gaussian lines, except for the strongest one (Fe XXV, 6.675 keV), are fixed at  $10^{-5}$  keV.